ELSEVIER

Computational Materials Science 29 (2004) 379–395

COMPUTATIONAL MATERIALS SCIENCE

www.elsevier.com/locate/commatsci

Nonlinear FE analysis of residual stresses induced by dislocations in heterostructures

Paweł Dłużewski [a,*], Grzegorz Maciejewski [a], Grzegorz Jurczak [a], Sławomir Kret [b], Jean-Yves Laval [c]

[a] *Institute of Fundamental Technological Research PAS, Swiętokrzyska 21, 00-049 Warsaw, Poland*
[b] *Institute of Physics PAS, Al. Lotników 32/36, 02-668 Warsaw, Poland*
[c] *Laboratoire de Physique du Solide—ESPCI CNRS UPR 05, 10 rue Vauquelin, 75231 Paris Cedex 05, France*

Received 18 September 2003; accepted 29 October 2003

Abstract

In this paper the field theory of dislocations is used in the finite element analysis of residual stresses in epitaxial layers. By digital processing of the HRTEM image of a GaAs/ZnTe/CdTe system the tensor maps of dislocation distribution are extracted. Such obtained maps are used as the input data to the finite element code. The mathematical foundations of this code are based on the compatibility equations for lattice distortions. The surface tension induced by misfit dislocations is considered here in terms of a 3D boundary-value problem for stress equilibrium in the interfacial zone. The numerical results show how strongly the surface tension depends on the nonlinear elastic behaviour of the crystal structure.

Keywords: Microscopy and microanalysis techniques; Nonlinear elasticity; Dislocation structure; Finite element analysis; Residual stresses; Layered structures

1. Introduction

High-resolution transmission electron microscopy (HRTEM) provides the possibility for quantitative measurement of lattice displacements within an accuracy of 0.03 Å, cf. [1]. On the other hand the strains obtained by digital processing of the HRTEM images reach considerably larger values than those measured at the micro- and macro-levels. In the GaAs/ZnTe/CdTe system analysed below the strains reach tens percent. In such a case the elastic nonlinearity takes a crucial role in the stress response of crystal structures. For example, the *linear* elasticity predicts equal sizes of the compression and extension regions around edge dislocation while the experimental evidence shows that the extension region, as being considerably more flexible, occupies a larger volume than the compressed one. In consequence, single dislocations change the volume of a crystal lattice. Over a few decades this volume effect was used by investigators to measure the dislocation density [2].

* Corresponding author. Tel.: +48-22-8261281; fax: +48-22-8269815.
E-mail address: pdluzew@ippt.gov.pl (P. Dłużewski).
URL: http://www.ippt.gov.pl/~pdluzew.

0927-0256/$ - see front matter © 2003 Elsevier B.V. All rights reserved.
doi:10.1016/j.commatsci.2003.10.012

The observed elastic nonlinearity is closely connected with the problem of the third-order elastic constants quantifying the asymmetry in the elastic compression/extension behaviour of real crystals. The problem of measuring this constants is more complicated than measuring of the classical (second-order) constants because their values depend on the strain measure used [3]. Nevertheless, the constants have been determined for hundreds of crystal structures [4–6].

The elastic nonlinearity is also responsible for many other phenomena observed experimentally. For instance the misfit dislocations expanding the crystal lattice lead to a planar expansion of interfacial zones and in consequence, lead to the bending of thin layers. In materials science this expansion is quantified in terms of a negative interfacial tension [7]. These nonlinear phenomena are beyond the scope of the linear theory of dislocations. The *linear* theory is widely used thanks to its efficiency in determining the analytical and numerical solutions. Nevertheless, to hold a linear character of differential equations, this theory by definition ignores all differences between the extension and compression behaviour of crystal lattice as well as cuts all geometrical differences between the actual and reference configurations. Obviously, in order to apply a nonlinear theory, the respective analytical or at least numerical tools have to be available. The problem is that constitutive models of nonlinear elastic behaviour of *anisotropic* solids generally available in FE codes are not suitable for solving the boundary-value problems for large deformation of dislocated crystals. For example, the most known anisotropic hyperelastic models (i.e. based on energy function), like the Saint-Venant–Kirchhoff and Biot models, behave just oppossed to real crystals. Namely, these models become stiff during extension and soft during compression [3]. Therefore, there exists a demand to use other nonlinear models which could be more adapted to the real elastic behaviour of crystal lattice.

In the last decade a whole spectrum of computational methods based on the *linear* theory of elasticity has been developed for the simulation of the dislocation movement. Many of these methods use *analytical* solutions for stresses and/or differential stress fields. In such a case two or more independent solutions for elemental stresses are used, e.g. the first solution concerns dislocations in an infinitely large continuum while the second concerns the proper boundary-value problem stated for a continuum free of dislocations. These two solutions are linked together according to the superposition rule which valid only in the linear theory. This simplified approach, called a discrete dislocation method, has achieved many interesting results concerning the computer animation of dislocation movement and formation of dislocation walls, cf. [8–12].

In this paper quite a different computational model is used. Contrary to the linear theory no superposition of elemental fields of strains, stresses nor differential stress functions are used here. The additive decomposition of the displacement gradient has been replaced by polar decomposition of the deformation gradient.

2. Atomic mappings and lattice distortions

A typical high quality image of a GaAs/ZnTe/CdTe interface is shown in Fig. 1. The image contrast in GaAs and CdTe is homogeneous—bright dots on dark background corresponding to

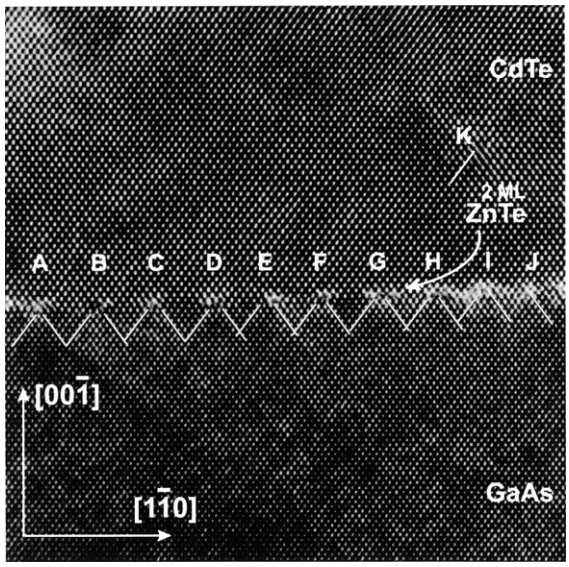

Fig. 1. HRTEM image of CdTe/ZnTe/GaAs structure.

the bi-atomic columns (Ga–As, Cd–Te). The interface (substrate surface) is tilted about 2° relatively to the crystallographic directions. Four mono-atomic steps are visible in the image. CdTe and GaAs have the same structure (sphalerite) with a lattice mismatch of 14.6%. Crystallographic misorientation of the CdTe film to the substrate was less than 1°. This misorientation was very small compared to the 6° disorientation reported by Cheng et al. [13] for the growth of CdTe directly on a GaAs substrate. Nine of the ten misfit dislocations situated on the interface are edge $\frac{1}{2}[1\,\bar{1}\,0]$. Their lines are parallel to the interfacial plane and perpendicular to the electron beam. Only one 60° dislocation is visible on the interface, see dislocation J. Its Burgers vector is $\frac{1}{2}[0\,\bar{1}\,\bar{1}]$ or $\frac{1}{2}[1\,0\,\bar{1}]$. The vector is deviated ±60° from the dislocation line lying in the $(1\,\bar{1}\,1)$ plane parallel to the electron beam. The second 60° dislocation is situated 8 nm above the interface, see dislocation K.

By means of the geometric phase method, the distribution of lattice distortions can be reconstructed from the HRTEM image. This method is based upon a centering of a small aperture around the strong reflection in the Fourier transform of the image, see [14]. The phase components give information about the local displacements of atomic planes. The geometric phase method is suitable to analyse distortions in strongly dislocated heterostructures. Applying two noncollinear Fourier components, a 2D piecewise continuous lattice displacement field $\hat{\mathbf{u}}(\mathbf{x})$ is determined. The lattice displacement field holds the same left- and right-handed derivatives on the discontinuity lines. Therefore, by computer processing of the HRTEM image it is also possible to extract a continuous distortion field $\boldsymbol{\beta}(\mathbf{x})$. Outside of the dislocation cores this field satisfies

$$\boldsymbol{\beta} = \frac{\partial \hat{\mathbf{u}}}{\partial \mathbf{x}}, \tag{1}$$

cf. Figs. 2 and 3. In our case, the lattice distortion field has been determined in relation to a perfect GaAs lattice. More details about such extracted distortion field are given in [15].

3. The nonlinear continuum theory of dislocations

Contrary to the atomic mappings discussed above the material mapping is assumed to be continuous and invertible. This invertibility was often ignored in the nonlinear continuum theory of dislocations (NCTD), cf. [16–18]. In consequence, NCTD was found as a theory closer more to the theories based on non-Riemannian geometries like cosmology and/or relativity than to a theory describing the real problems of dislocations

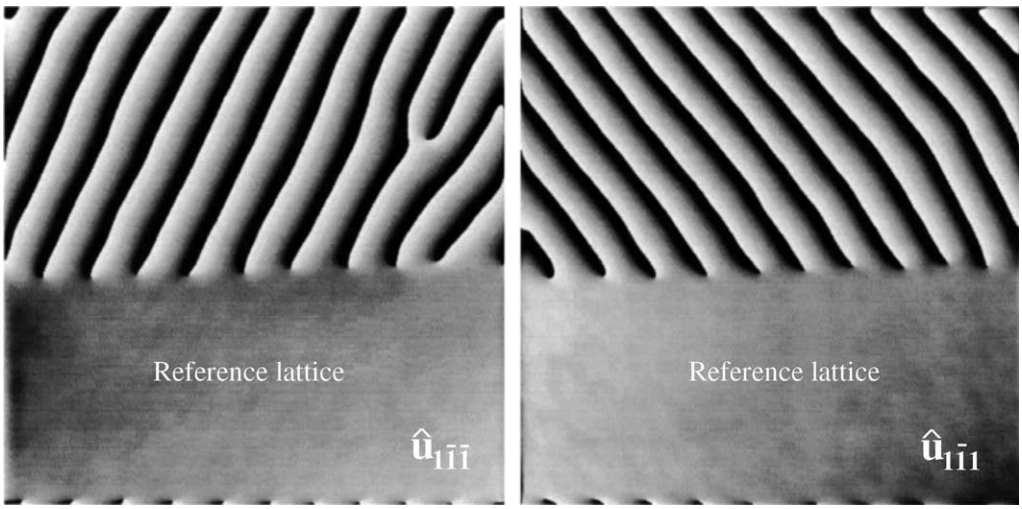

Fig. 2. Piecewise continuous lattice displacement field $\hat{\mathbf{u}}(\mathbf{x})$ obtained by digital processing of the HRTEM image shown in Fig. 1.

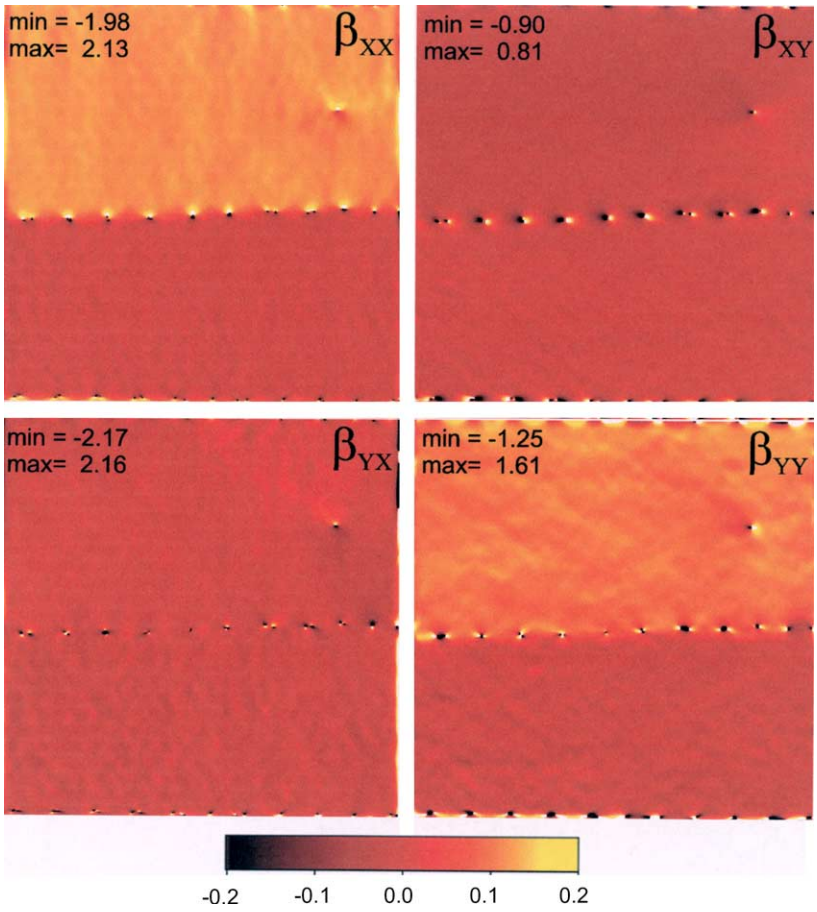

Fig. 3. Continuous lattice distortion field $\boldsymbol{\beta}(\mathbf{x})$ obtained from the HRTEM image shown in Fig. 1.

in crystal structures. Therefore, let us reconsider the fundamental relations resulting from the materials mapping applied in our paper. The total deformation gradient $\mathbf{F}$ in a positively oriented Euclidean space E^3 has to satisfy the following integrability conditions

$$\operatorname{curl}\mathbf{F}^{-1} = \mathbf{0}, \tag{2}$$

and equivalently

$$\operatorname{CURL}\mathbf{F} = \mathbf{0}, \tag{3}$$

where curl and CURL denote the curl operators related to the current and reference configurations, respectively. The conditions rewritten in the index notation corresponding to curvilinear coordinate sets $\{x^k\}$ and $\{X^K\}$ take the form

$$\overset{-1}{F}{}^{K}{}_{l,m}e^{lm}{}_{n} = 0, \tag{4}$$

$$F^{k}{}_{L,M}e^{LM}{}_{N} = 0, \tag{5}$$

where the comma denotes the covariant derivative, while $e^{km}{}_{n}$ and $e^{KM}{}_{N}$ are representations of the alternating tensor, see Appendix A.1.

Identities yielding from compatibility conditions are obtained by substituting $\mathbf{F} = \mathbf{F}_{\mathrm{lt}}\mathbf{F}_{\mathrm{pl}}$ into (3), giving

$$\operatorname{grad}\mathbf{F}_{\mathrm{pl}}^{-1}\dot{\times}\mathbf{F}_{\mathrm{lt}}^{-1} + \mathbf{F}_{\mathrm{pl}}^{-1}\operatorname{curl}\mathbf{F}_{\mathrm{lt}}^{-1} = \mathbf{0}, \tag{6}$$

$$\operatorname{GRAD}\mathbf{F}_{\mathrm{lt}}\dot{\times}\mathbf{F}_{\mathrm{pl}} + \mathbf{F}_{\mathrm{lt}}\operatorname{CURL}\mathbf{F}_{\mathrm{pl}} = \mathbf{0}, \tag{7}$$

where $\dot{\times}$ denotes a double product over two neighboring indices—the scalar one over the firsts

and the cross one over the second indices, cf. Appendix A.2 where the operator $\dot{\times}$ is used in the index notation. Such decomposition is valid also in any non-Euclidean (non-Riemannian) space, provided that the respective differential condition establishing the distant parallelism is satisfied. Note that the mentioned compatibility conditions can also be rewritten in the form

$$\operatorname{curl}\mathbf{F}_{\mathrm{lt}}^{-1}+\mathbf{F}_{\mathrm{pl}}\operatorname{grad}\mathbf{F}_{\mathrm{pl}}^{-1}\dot{\times}\mathbf{F}_{\mathrm{lt}}^{-1}=\mathbf{0}, \tag{8}$$

$$\operatorname{CURL}\mathbf{F}_{\mathrm{pl}}+\mathbf{F}_{\mathrm{lt}}^{-1}\operatorname{GRAD}\mathbf{F}_{\mathrm{lt}}\dot{\times}\mathbf{F}_{\mathrm{pl}}=\mathbf{0}. \tag{9}$$

Identities yielding from invertibility conditions are obtained from differentiation of $\mathbf{F}\mathbf{F}^{-1}=\mathbf{F}_{\mathrm{lt}}\mathbf{F}_{\mathrm{lt}}^{-1}=\mathbf{F}_{\mathrm{pl}}\mathbf{F}_{\mathrm{pl}}^{-1}=\mathbf{1}$. Differentiation of the mentioned identities over coordinates from the current and reference configurations gives respectively

$$\operatorname{grad}\mathbf{F}_{\mathrm{lt}}\mathbf{F}_{\mathrm{lt}}^{-1}=-\mathbf{F}_{\mathrm{lt}}\operatorname{grad}\mathbf{F}_{\mathrm{lt}}^{-1}, \tag{10}$$

$$\operatorname{GRAD}\mathbf{F}_{\mathrm{lt}}\mathbf{F}_{\mathrm{lt}}^{-1}=-\mathbf{F}_{\mathrm{lt}}\operatorname{GRAD}\mathbf{F}_{\mathrm{lt}}^{-1}, \tag{11}$$

$$\operatorname{grad}\mathbf{F}_{\mathrm{pl}}\mathbf{F}_{\mathrm{pl}}^{-1}=-\mathbf{F}_{\mathrm{pl}}\operatorname{grad}\mathbf{F}_{\mathrm{pl}}^{-1}, \tag{12}$$

$$\operatorname{GRAD}\mathbf{F}_{\mathrm{pl}}\mathbf{F}_{\mathrm{pl}}^{-1}=-\mathbf{F}_{\mathrm{pl}}\operatorname{GRAD}\mathbf{F}_{\mathrm{pl}}^{-1}. \tag{13}$$

Additionally, pseudo-operators Grad and Curl are introduced by expressing the differentiation over the lattice reference configuration. Namely, for an arbitrarily chosen tensor field, say $\mathbf{t}(\mathbf{x}(\mathbf{X}))$, the pseudo-operators denote the following differentiation

$$\begin{aligned}\operatorname{Grad}\mathbf{t}&\overset{df}{=}\mathbf{t}_{,k}F_{\mathrm{lt}}^{-1\,k}{}_{K}\otimes\mathbf{E}^{K}=\mathbf{t}_{,K}\overset{-1}{F}{}_{\mathrm{pl}}^{K}{}_{M}\otimes\mathbf{E}^{M}\\&=\mathbf{t}_{,K}\overset{-1}{F}{}_{\mathrm{pl}}^{K}{}_{m}\otimes\mathbf{e}^{m},\end{aligned} \tag{14}$$

$$\begin{aligned}\operatorname{Curl}\mathbf{t}&\overset{df}{=}\mathbf{t}_{,k}F_{\mathrm{lt}}^{-1\,k}{}_{K}\times\mathbf{E}^{K}=\mathbf{t}_{,K}\overset{-1}{F}{}_{\mathrm{pl}}^{K}{}_{M}\times\mathbf{E}^{M}\\&=\mathbf{t}_{,K}\overset{-1}{F}{}_{\mathrm{pl}}^{K}{}_{m}\times\mathbf{e}^{m},\end{aligned} \tag{15}$$

where

$$\begin{aligned}\mathbf{t}_{,k}&=\frac{\partial}{\partial x^{k}}\left(t^{ij}\mathbf{e}_{i}\otimes\mathbf{e}_{j}\right)\\&=\left(\frac{\partial t^{ij}}{\partial x^{k}}+t^{lj}\Gamma_{lk}{}^{i}+t^{il}\Gamma_{lk}{}^{j}\right)\mathbf{e}_{i}\otimes\mathbf{e}_{j}.\end{aligned}$$

Geometrical relations between $\Gamma_{kl}{}^{m}$, $\Gamma_{KL}{}^{M}$ and $\mathbf{F}_{,K}$ are shown in Appendix A.1. These look quite different than those used by Kondo [16,18] and Bilby [17] because of the use of different metrics. We use the Euclidean space metric and connection rewritten in immobile curvilinear coordinate sets $\{x^{k}\}$ and $\{X^{K}\}$ called the Eulerian and Lagrangian coordinate sets. The authors mentioned used a set convected or rather deformed together with an imagined material space in which the distances were determined by lattice metrics. Obviously, these fundamental difference in geometrical tools used makes no difference on constitutive modelling. Therefore, constitutive equations formulated correctly by means of one tool can be successfully rewritten in terms of the second tool.

True Burgers vector can be determined by drawing a respective Burgers circuit in the current or in the lattice reference configuration, cf. the FS/RH and SF/RH methods described by Hirth and Lothe [19]. The first method (finish-start/right-handed) consists in drawing the enclosed circle in the actual configuration to find the Burgers vector in the lattice reference configuration, see Fig. 1.21 in the mentioned textbook. Obviously, the result of this operation depends not only on the method chosen (FS/RH or SF/RH) but also on the assumed sense of dislocation line. In materials science the unit vector of dislocation line $\boldsymbol{\xi}$ is taken often to be "point into the paper", see Fig. 1.22 in [19]. On the other hand, for RH coordinate systems, the sense of the oriented arc segment used in the Stokes theorem is counter-clockwise, which means that the infinitesimal vector of an area element satisfies $\mathrm{d}\mathbf{s}=-\boldsymbol{\xi}\,\mathrm{d}s$. Therefore, for the FS/RH method corresponding to the sense of dislocation line directed "point into the paper" and to the clockwise Burgers circuit $C^{\mathbf{x}}_{\mathbf{x}_0}$, see Fig. 1.20 in [19], we find

$$\begin{aligned}\hat{\mathbf{b}}&=-\oint_{C^{\mathbf{x}}_{\mathbf{x}_0}}\mathbf{F}_{\mathrm{lt}}^{-1}\,\mathrm{d}\mathbf{x}=\int_{S}\operatorname{curl}\mathbf{F}_{\mathrm{lt}}^{-1}\,\mathrm{d}\mathbf{s}=\int_{S}\tilde{\boldsymbol{\alpha}}\,\mathrm{d}\mathbf{s}\\&=-\int_{S}\tilde{\boldsymbol{\alpha}}\boldsymbol{\xi}\,\mathrm{d}s,\end{aligned} \tag{16}$$

where

$$\tilde{\boldsymbol{\alpha}}\overset{df}{=}\operatorname{curl}\mathbf{F}_{\mathrm{lt}}^{-1}. \tag{17}$$

Note that contrary to the Burgers vector, the dislocation distribution (DD) tensor $\tilde{\boldsymbol{\alpha}}$ is invariant with respect to the assumed sense of dislocation line, cf. (16). The true Burgers vector determines components of dislocation with reference to undeformed crystal lattice. Differential forms of the Burgers vectors and the area elements satisfy the well-known transformation rules

$$\mathrm{d}\mathbf{b} = \mathbf{F}_{\mathrm{lt}}\,\mathrm{d}\hat{\mathbf{b}}, \tag{18}$$

$$\mathrm{d}\mathbf{s} = \mathbf{F}_{\mathrm{lt}}^{-\mathrm{T}}\,\mathrm{d}\hat{\mathbf{s}}\det\mathbf{F}_{\mathrm{lt}}. \tag{19}$$

Substitution into (16) gives the following differential relations

$$\mathrm{d}\mathbf{b} = \boldsymbol{\alpha}\,\mathrm{d}\mathbf{s}, \tag{20}$$

$$\mathrm{d}\hat{\mathbf{b}} = \hat{\boldsymbol{\alpha}}\,\mathrm{d}\hat{\mathbf{s}}, \tag{21}$$

where

$$\boldsymbol{\alpha} \overset{df}{=} \mathbf{F}_{\mathrm{lt}}\operatorname{curl}\mathbf{F}_{\mathrm{lt}}^{-1}, \tag{22}$$

$$\hat{\boldsymbol{\alpha}} \overset{df}{=} \operatorname{curl}\mathbf{F}_{\mathrm{lt}}^{-1}\mathbf{F}_{\mathrm{lt}}^{-\mathrm{T}}\det\mathbf{F}_{\mathrm{lt}}, \tag{23}$$

cf. (17), $\boldsymbol{\alpha}$ represents the spatial distribution of the spatial Burgers vector, while $\hat{\boldsymbol{\alpha}}$ specifies the local distribution of the true Burgers vector in the lattice reference configuration. Summing up, the DD tensors hold the following transformation rule

$$\boldsymbol{\alpha} = \mathbf{F}_{\mathrm{lt}}\tilde{\boldsymbol{\alpha}} = \mathbf{F}_{\mathrm{lt}}\hat{\boldsymbol{\alpha}}\mathbf{F}_{\mathrm{lt}}^{\mathrm{T}}\det\mathbf{F}_{\mathrm{lt}}^{-1}. \tag{24}$$

Note that the same transformation rule holds for the Cauchy and Piola–Kirchhoff stress tensors. Due to compatibility conditions, the DD tensors can be determined uniquely by means of mutually different derivatives. Using the identity transformations for deformation gradients, we find the following formulae equivalent to (22)

$$\boldsymbol{\alpha} = \operatorname{grad}\mathbf{F}_{\mathrm{lt}}\dot{\times}\mathbf{F}_{\mathrm{lt}}^{-1} \tag{25}$$

$$= \mathbf{F}_{\mathrm{lt}}\mathbf{F}_{\mathrm{pl}}\operatorname{grad}\mathbf{F}_{\mathrm{pl}}^{-1}\dot{\times}\mathbf{F}_{\mathrm{lt}}^{-1} \tag{26}$$

$$= -F_{\mathrm{lt}}\operatorname{grad}\mathbf{F}_{\mathrm{pl}}\dot{\times}(\mathbf{F}_{\mathrm{lt}}\mathbf{F}_{\mathrm{pl}})^{-1}, \tag{27}$$

$$\hat{\boldsymbol{\alpha}} = -\operatorname{Grad}\mathbf{F}_{\mathrm{lt}}^{-1}\dot{\times}\mathbf{F}_{\mathrm{lt}} \tag{28}$$

$$= -\mathbf{F}_{\mathrm{lt}}^{-1}\operatorname{Curl}\mathbf{F}_{\mathrm{lt}} \tag{29}$$

$$= -\mathbf{F}_{\mathrm{pl}}\operatorname{Curl}\mathbf{F}_{\mathrm{pl}}^{-1} \tag{30}$$

$$= -\operatorname{Grad}\mathbf{F}_{\mathrm{pl}}\dot{\times}\mathbf{F}_{\mathrm{pl}}^{-1} \tag{31}$$

$$= \operatorname{CURL}\mathbf{F}_{\mathrm{pl}}\mathbf{F}_{\mathrm{pl}}^{\mathrm{T}}\det\mathbf{F}_{\mathrm{pl}}^{-1}, \tag{32}$$

see Appendix A.2. Most of the indentities were derived in 1995/1996 by Dłużewski [20,21]. In the numerical code presented in Section 5, the relations (29), (30) and (32) play the important role.

Contrary to $\tilde{\boldsymbol{\alpha}}(\mathbf{X})$, the field $\hat{\boldsymbol{\alpha}}(\mathbf{X})$ is *invariant* with respect to any self-compatible elastic deformation, i.e. replacing $\mathbf{F}_{\mathrm{lt}}$ by $\mathbf{F}'_{\mathrm{lt}} = \mathbf{F}_{\mathrm{lt}} + \operatorname{Grad}\mathbf{u}'$ in (23) we find the same tensor field $\hat{\boldsymbol{\alpha}}(\mathbf{X})$ as that determined for $\mathbf{F}_{\mathrm{lt}}$.

Spatial Burgers vector (see Fig. 1.20 in [19]). In this case, the closed Burgers circuit is drawn in the lattice reference configuration. Its unclosed trace from the actual configuration determines the spatial Burgers vector. According to the NCTD, we can determine the actual and lattice reference configurations to be open sets in E^3. For any curve segment $C^{\mathbf{x}}_{\mathbf{x}_0}$ connecting arbitrarily chosen points $\mathbf{x}_0$ and $\mathbf{x}$ in the actual configuration, the function $\mathbf{F}_{\mathrm{lt}}^{-1}(x)$ determines uniquely a continuous and *invertible* mapping

$$\hat{\mathbf{x}}(\mathbf{x})|_{C^{\mathbf{x}}_{\mathbf{x}_0}} = \int_{C^{\mathbf{x}}_{\mathbf{x}_0}} \mathbf{F}_{\mathrm{lt}}^{-1}\,\mathrm{d}\mathbf{x}', \tag{33}$$

which determines an oriented curve segment being a trace of the Burgers circuit in the lattice reference configuration, cf. Fig. 4(b). In the continuum theory of dislocations this relation corresponds to the following formula for the spatial Burgers vector

$$\mathbf{b} = \oint_{\widehat{C}^{\hat{\mathbf{x}}}_{\hat{\mathbf{x}}_0}} \mathbf{F}_{\mathrm{lt}}\,\mathrm{d}\hat{\mathbf{x}} = -\int_{\widehat{S}} \operatorname{Curl}\mathbf{F}_{\mathrm{lt}}\,\mathrm{d}\hat{\mathbf{s}}$$

$$= \int_{\widehat{S}} \operatorname{Curl}\mathbf{F}_{\mathrm{lt}}\hat{\boldsymbol{\xi}}\,\mathrm{d}\hat{s}, \tag{34}$$

where $\widehat{S}$ denotes the surface bounded by a clockwise Burgers circuit $\widehat{C}^{\hat{\mathbf{x}}}_{\hat{\mathbf{x}}_0}$ in the lattice reference configuration.

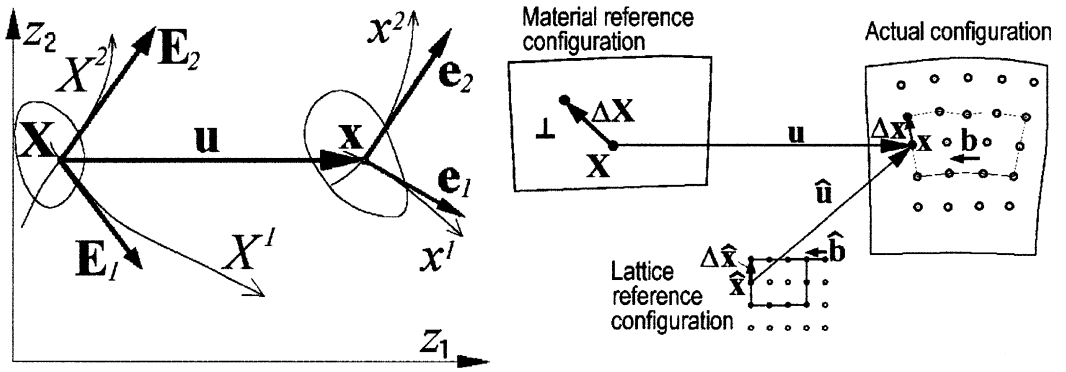

Fig. 4. Coordinate systems versus reference configurations.

4. Nonlinear elasticity

Let us assume that the specific free energy of a crystal structure is governed by the following constitutive relation:

$$\psi = \psi_{\mathrm{h}}(\hat{\boldsymbol{\varepsilon}}_{\mathrm{h}}, \hat{\boldsymbol{\alpha}}_{\mathrm{h}}, x_1, \ldots, x_n, T), \tag{35}$$

where T denotes temperature, $x_1, \ldots, x_n$ means the mole fractions of elements, and $\hat{\boldsymbol{\varepsilon}}_{\mathrm{h}}$ is a heterostructural strain. The strain is a nonlinear function of the lattice deformation measured in relation to a fixed lattice reference structure (GaAs) and $\hat{\boldsymbol{\alpha}}_{\mathrm{h}}$ is a nonlinear function of both $\mathbf{F}_{\mathrm{lt}}$ and $\operatorname{grad}\mathbf{F}_{\mathrm{lt}}$, i.e. $\hat{\boldsymbol{\varepsilon}}_{\mathrm{h}} = \hat{\boldsymbol{\varepsilon}}_{\mathrm{h}}(\mathbf{F}_{\mathrm{lt}})$, $\hat{\boldsymbol{\alpha}}_{\mathrm{h}} = \hat{\boldsymbol{\alpha}}_{\mathrm{h}}(\mathbf{F}_{\mathrm{lt}}, \operatorname{grad}\mathbf{F}_{\mathrm{lt}})$. The structure shown in Fig. 1 can be considered as a threefold lattice dilute $\mathrm{Cd}_x\mathrm{Zn}_y\mathrm{Ga}_{1-x-y}\mathrm{Te}_z\mathrm{As}_{1-z}$ corresponding to $\psi = \psi(\hat{\boldsymbol{\varepsilon}}_{\mathrm{h}}, \hat{\boldsymbol{\alpha}}_{\mathrm{h}}, x, y, z, T)$. Nevertheless, assuming that the system is composed of sequential layers GaAs/ZnTe/CdTe it is convenient to introduce a lattice reference structure for each of layers, independently. This means that for a given layer with a homogeneous chemical composition, (35) can be replaced by

$$\psi = \psi(\hat{\boldsymbol{\varepsilon}}, \hat{\boldsymbol{\alpha}})|_{x_1,\ldots,x_n,T=\mathrm{const}}, \tag{36}$$

where $\hat{\boldsymbol{\varepsilon}} = \hat{\boldsymbol{\varepsilon}}(\mathbf{F}_{\mathrm{lt}'}), \hat{\boldsymbol{\alpha}} = \hat{\boldsymbol{\alpha}}(\mathbf{F}_{\mathrm{lt}'}, \operatorname{grad}\mathbf{F}_{\mathrm{lt}'})$ and $\mathbf{F}_{\mathrm{lt}'} = \mathbf{F}_{\mathrm{lt}}\mathbf{F}_{\mathrm{ch}}^{-1}$.

Summing up, we use the following decomposition of the total deformation gradient

$$\mathbf{F} = \underbrace{\overbrace{\mathbf{R}\mathbf{U}}^{\mathbf{F}_{\mathrm{lt}'}}\mathbf{F}_{\mathrm{ch}}}_{\mathbf{F}_{\mathrm{lt}}}\mathbf{F}_{\mathrm{pl}}, \tag{37}$$

where $\mathbf{R}$ and $\mathbf{U}$ denote the rotation and stretch determined in relation to a stress-free configuration of the crystal lattice with actual chemical composition, while $\mathbf{F}_{\mathrm{ch}}$ denotes the chemical deformation between two stress-free configurations differing in chemical composition, i.e. corresponding to the actual and reference compositions. The reference composition was assumed to determine uniquely the lattice distortion maps for the whole heterostructure, see Fig. 3.

4.1. Elasticity of perfect crystal lattice

The elastic nonlinearity of real crystals makes the compression harder than extension. Therefore, many attempts are made to predict this effect in mathematical terms. For many crystal structures the third-order elastic constants have been investigated, see tabulated constants by Hiki and Granato [22], Drabble and Brammer [23], Vaidya and Kennedy [4,5], Teodosiu [24] among others. Most of the experimental results were obtained by using the Green strain, also called the Lagrangian strain. Unfortunately, it turns out that such determined constants depend very strongly on the strain measure used, see Table II in Dłużewski [3]. Therefore, it is convenient to use another, more general definition of the Lagrangian strain.

Definition 1. By a Lagrangian strain we mean the following tensor function

$$\hat{\boldsymbol{\varepsilon}} \overset{\mathrm{df}}{=} f(u_{\mathrm{l}})\mathbf{u}_{\mathrm{l}} \otimes \mathbf{u}_{\mathrm{l}}, \tag{38}$$

where u_{I} and $\mathbf{u}_{\mathrm{I}}$ denote respectively the Ith eigenvalue and unit eigenvector of the stretch tensors, while $f(\cdot)$ denotes an arbitrarily chosen C^1 monotonically increasing function $f(x): R^+ \ni x \to f \in R$ which satisfies the conditions $f(x)|_{x=1} = 0$ and $\frac{\mathrm{d}f(x)}{\mathrm{d}x}|_{x=1} = 1$.

This definition includes the well-known family of strains [25,26]

$$\hat{\boldsymbol{\varepsilon}} \overset{\mathrm{d}f}{=} \begin{cases} \frac{1}{m}(\mathbf{U}^m - \mathbf{1}) & \text{for } m \neq 0, \\ \ln \mathbf{U} & \text{for } m = 0. \end{cases} \tag{39}$$

In a similar way a family of Eulerian strain measures dependent on the left Cauchy–Green stretch tensor can be defined. Supposing that the specific free energy depends on the Lagrangian strain and temperature,

$$\psi = \psi(\hat{\boldsymbol{\varepsilon}}, T), \tag{40}$$

it can be proven [3] that the Cauchy stress is governed by the following equation

$$\boldsymbol{\sigma} = \mathbf{R}\left(\widehat{\mathscr{A}} : \hat{\rho}\frac{\partial \psi}{\partial \hat{\boldsymbol{\varepsilon}}}\right)\mathbf{R}^{\mathrm{T}} \det \mathbf{F}^{-1}, \tag{41}$$

where $\hat{\rho}$ denotes the mass density in the reference configuration. The fourth-order tensor $\widehat{\mathscr{A}}$, decomposed in the eigenvector basis $\{\mathbf{u}_{\mathrm{I}}\}$, has the following nonvanishing components

$$\widehat{\mathscr{A}}_{\mathrm{IJIJ}} = \widehat{\mathscr{A}}_{\mathrm{IJJI}} = \begin{cases} \delta_{\mathrm{IJ}} u_{\mathrm{I}} f'(u_{\mathrm{I}}) & \text{for } u_{\mathrm{I}} = u_{\mathrm{J}}, \\ \frac{u_{\mathrm{I}} u_{\mathrm{J}}[f(u_{\mathrm{I}}) - f(u_{\mathrm{J}})]}{u_{\mathrm{I}}^2 - u_{\mathrm{J}}^2} & \text{for } u_{\mathrm{I}} \neq u_{\mathrm{J}}, \end{cases} \tag{42}$$

where $f'(u_{\mathrm{I}}) = \frac{\mathrm{d}f(u)}{\mathrm{d}u}|_{u=u_{\mathrm{I}}}$. For example, in the case of logarithmic strain, see (39), we find

$$\widehat{\mathscr{A}}_{\mathrm{IJIJ}} = \begin{cases} \delta_{\mathrm{IJ}} & \text{for } \hat{\varepsilon}_{\mathrm{I}} = \hat{\varepsilon}_{\mathrm{J}}, \\ \frac{(\hat{\varepsilon}_{\mathrm{I}} - \hat{\varepsilon}_{\mathrm{J}})}{e^{\hat{\varepsilon}_{\mathrm{I}} - \hat{\varepsilon}_{\mathrm{J}}} - e^{\hat{\varepsilon}_{\mathrm{I}} - \hat{\varepsilon}_{\mathrm{J}}}} & \text{for } \hat{\varepsilon}_{\mathrm{I}} \neq \hat{\varepsilon}_{\mathrm{J}}. \end{cases} \tag{43}$$

Let us assume here that an elastic crystal satisfies the following specific strain energy function

$$\psi(\hat{\boldsymbol{\varepsilon}}) = \frac{1}{\hat{\rho}}\left[\frac{1}{2!}\hat{c}^{ijkl}\hat{\varepsilon}_{ij}\hat{\varepsilon}_{kl} + \frac{1}{3!}\hat{c}^{ijklmn}\hat{\varepsilon}_{ij}\hat{\varepsilon}_{kl}\hat{\varepsilon}_{mn}\right], \tag{44}$$

where $\hat{\mathbf{c}}$ and $\widehat{\mathbf{C}}$ are the second- and third-order elastic tensors determined in relation to a given strain measure. Substituting (44) into (41) the following stress–strain relation for the elastic behaviour of a crystal lattice is found

$$\boldsymbol{\sigma} = \mathbf{R}\left[\widehat{\mathscr{A}} : \left(\hat{\mathbf{c}} : \hat{\boldsymbol{\varepsilon}} + \frac{1}{2}\hat{\boldsymbol{\varepsilon}} : \widehat{\mathbf{C}} : \hat{\boldsymbol{\varepsilon}}\right)\right]\mathbf{R}^{\mathrm{T}} \det \mathbf{F}^{-1}. \tag{45}$$

Contrary to the second-order constants the values of third-order ones are strongly dependent on the strain measure used, see Dłużewski [3]. Moreover, the constants can be recalculated mutually reversible for any other strain measure. In practice, most third-order constants were determined experimentally in relation to the Green strain, see [22,27–29]. Assuming two different strain measures, say dependent on two different strain parameters m and m' (39) we find a mutually reversible tensor function $\hat{\boldsymbol{\varepsilon}}' = \hat{\boldsymbol{\varepsilon}}'(\hat{\boldsymbol{\varepsilon}})$. In other words, if we have components of strain referred to the Green strain measure then we can recalculate them uniquely for the logarithmic strain. Using the transformation rule derived by Dłużewski [3] we find for cubic systems

$$\begin{aligned}
\widehat{C}'_{111} &= \widehat{C}_{111} + (m - m')3\hat{c}_{11}, \\
\widehat{C}'_{112} &= \widehat{C}_{112} + (m - m')\hat{c}_{12}, \\
\widehat{C}'_{123} &= \widehat{C}_{123}, \\
\widehat{C}'_{144} &= \widehat{C}_{144} + (m - m')\tfrac{1}{2}\hat{c}_{12}, \\
\widehat{C}'_{155} &= \widehat{C}_{155} + (m - m')\left[\hat{c}_{44} + \tfrac{1}{4}\hat{c}_{12} + \tfrac{1}{4}\hat{c}_{11}\right], \\
\widehat{C}'_{456} &= \widehat{C}_{456} + (m - m')\tfrac{3}{4}\hat{c}_{44}.
\end{aligned} \tag{46}$$

In the above equation the Voight notation reducing the number of subscripts has been used: $11 \to 1$, $22 \to 2$, $33 \to 3$, $23 \to 4$, $13 \to 5$, $12 \to 6$, e.g. $\widehat{C}_{111231} \to \widehat{C}_{165}$. Applying (46) to the elastic constants for GaAs, ZnTe and CdTe we can recalculate the constants referred to the Green strain ($m = 2$) to those corresponding to the logarithmic strain ($m = 0$), see Table 1. Note that, if third-order constants related to a given strain measure vanishes, then after recalculation, nonzero values for other measures are obtained, cf. (46) and Table 1.

4.2. Elasticity of dislocated crystal lattice

The real stiffness of disordered regions is lower than that of a perfect lattice in which all molecules

Table 1
Second and third-order elastic constants [GPa] related to the Green and logarithmic strain measures

m	c_{11}	c_{12}	c_{44}	C_{111}	C_{112}	C_{123}	C_{144}	C_{155}	C_{456}	Expl.
CdTe										
2	54	37	16	−213	−210	−42	14	−65	5	[29]
0	54	37	16	111	−136	−42	51	13	29	
ZnTe										
2	71	41	31	−779	−649	−267	−132	−473	−34	[34]
0	71	41	31	−352	−568	−267	−91	−355	13	
GaAs										
2	119	54	60	−675	−402	−4	−70	−320	−69	[23]
0	119	54	60	39	−294	−4	−16	−113	21	

tend consistently to the same configuration. To take into account the stiffness reduction in the lattice disordered regions the following constitutive equation is assumed

$$\boldsymbol{\sigma} = \mathbf{R}\left[\widehat{\mathscr{A}} : \left(e^{-r\hat{\alpha}}\hat{\mathbf{c}} : \hat{\boldsymbol{\varepsilon}} + \tfrac{1}{2}e^{-2r\hat{\alpha}}\hat{\boldsymbol{\varepsilon}} : \widehat{\mathbf{C}} : \hat{\boldsymbol{\varepsilon}}\right)\right]\mathbf{R}^{\mathrm{T}} \det \mathbf{F}^{-1}, \tag{47}$$

where $\hat{\alpha}$ is the second invariant of the true DD tensor. In our approach r denotes a coefficient responsible for the assumed reduction of elastic stiffness in lattice disordered regions, see Figs. 5 and 6. The DD tensor field extracted from the HRTEM image has strongly localised peaks in these regions. Outside the peaks the field $\hat{\boldsymbol{\alpha}}(\mathbf{x})$ vanishes.

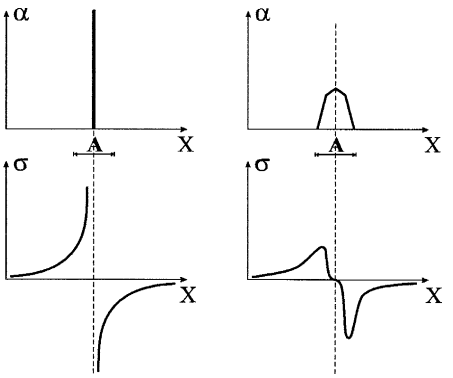

Fig. 5. Schematic diagram of stress distribution about edge dislocation: (a) discrete dislocation in the linear elastic continuum, (b) FE distributed core in nonlinear elastic continuum.

5. Finite element analysis

Let the lattice configuration visible in Fig. 1 be the *material reference* configuration. On the other hand, by the *lattice reference* configuration we assume a perfect lattice GaAs, ZnTe or CdTe depending on the layer. The total deformation gradient decomposes into

$$\mathbf{F} = \mathbf{F}_{\mathrm{lt}'}\mathbf{F}_{\mathrm{ch}}\mathbf{F}_{\mathrm{o}}^{-1}, \tag{48}$$

where $\mathbf{F}_{\mathrm{o}}^{-1}$ is the source deformation transforming locally the initial (HRTEM) configuration to the reference lattice (GaAs) assumed to determine the lattice distortion field for the entire heterostructure, see Fig. 3. $\mathbf{F}_{\mathrm{lt}'}$ includes the lattice rotation and stretch measured in relation to the stress-free configuration of the lattice with actual chemical composition, GaAs, ZnTe or CdTe depending on the layer.

Chemical deformation tensor describes the difference between two stress-free configurations corresponding respectively: to the actual chemical composition of layer (e.g. CdTe) and to the reference chemical composition (GaAs) chosen to measure the lattice distortion distribution in the entire heterostructure as shown in Fig. 3. Due to the cubic symmetry of the lattice, this tensor takes the isotropic form

$$\mathbf{F}_{\mathrm{ch}}(\mathbf{x}) = \frac{\hat{a}(\mathbf{x})}{\hat{a}_{\mathrm{Ref}}}1, \tag{49}$$

where $\hat{a}$ and $\hat{a}_{\mathrm{Ref}}$ denote the lattice parameters of a perfect lattice corresponding to the actual and reference chemical compositions, respectively. By

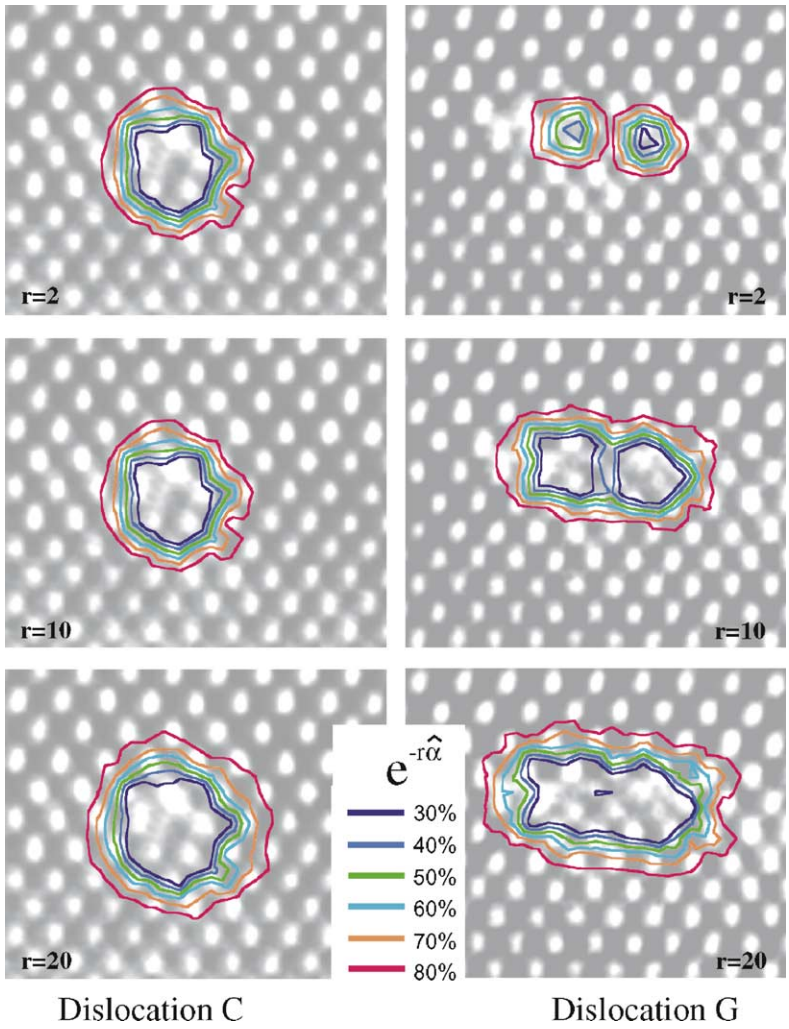

Fig. 6. The maps of elastic stiffness factor $e^{-r\hat{\alpha}}$ simulated for various dislocation core coefficient r.

a lattice reference parameter is meant here $\hat{a}_{\mathrm{Ref}} \equiv \hat{a}_{\mathrm{GaAs}}$ while the function $\hat{a}(\mathbf{x})$ takes the values $\hat{a}_{\mathrm{GaAs}}$, $\hat{a}_{\mathrm{ZnTe}}$, $\hat{a}_{\mathrm{CdTe}}$ depending of the layer. For instance in the CdTe layer the actual lattice vector $\mathbf{a}$ satisfies the transformation rule

$$\mathbf{a} = \mathbf{F}_{\mathrm{lt}'}\hat{\mathbf{a}}_{\mathrm{CdTe}} = \mathbf{F}_{\mathrm{lt}}\hat{\mathbf{a}}_{\mathrm{GaAs}}, \tag{50}$$

where $\hat{\mathbf{a}}_{\mathrm{GaAs}}$ and $\hat{\mathbf{a}}_{\mathrm{CdTe}}$ denote the same crystallographic vector determined respectively in relation to different stress-free configurations corresponding to GaAs and CdTe, respectively.

The source and total deformation tensors can be related respectively to the distortion field $\boldsymbol{\beta}^{\mathrm{HRTEM}}(\mathbf{x}^{\mathrm{HRTEM}})$ observed under HRTEM and to the material displacement vector field $\mathbf{u}(\mathbf{x})$ by the following relations

$$\mathbf{F}_{\mathrm{o}}^{-1} = 1 - \boldsymbol{\beta}^{\mathrm{HRTEM}}, \tag{51}$$

$$\mathbf{F}^{-1} = 1 - \nabla\mathbf{u} = \frac{\partial(\mathbf{x}-\mathbf{u})}{\partial\mathbf{x}} = \frac{\partial\mathbf{x}^{\mathrm{HRTEM}}}{\partial\mathbf{x}}. \tag{52}$$

The source deformation tensor $\mathbf{F}_{\mathrm{o}}$ can also be related to the following lattice distortion tensor

$$\hat{\boldsymbol{\beta}} \overset{df}{=} (1 - \boldsymbol{\beta}^{\mathrm{HRTEM}})^{-1} - \mathbf{1}, \tag{53}$$

which satisfies

$$\mathbf{F}_{\mathrm{o}} = \mathbf{1} + \hat{\boldsymbol{\beta}}. \tag{54}$$

Lattice rebuilding tensor—a dilemma whether the source deformation tensor $\mathbf{F}_{\mathrm{o}}$ should be treated as an initial elastic deformation $\mathbf{F}_{\mathrm{lt}_{\mathrm{o}}}$ or as an inverse of a certain lattice rebuilding plastic deformation tensor, say $\mathbf{F}^{-1}_{\mathrm{pl}_{\mathrm{o}}}$, comprises a long-standing problem. In practice, both interpretations reduce themselves to the same multiplicative decomposition, in which $\mathbf{F}_{\mathrm{pl}_{\mathrm{o}}}$ or $\mathbf{F}^{-1}_{\mathrm{lt}_{\mathrm{o}}}$ takes quite the same role of a complementary deformation to $\mathbf{F}_{\mathrm{lt}}$. Note that independently of the interpretation assumed, all relations previously derived for compatibility conditions between $\mathbf{F}_{\mathrm{lt}}$ and $\mathbf{F}_{\mathrm{pl}}$ hold true. The use of $\mathbf{F}_{\mathrm{pl}_{\mathrm{o}}}$ or $\mathbf{F}^{-1}_{\mathrm{lt}_{\mathrm{o}}}$ depends on the preferences of a given author. We assume here that $\mathbf{F}^{-1}_{\mathrm{o}} \equiv \mathbf{F}_{\mathrm{pl}_{\mathrm{o}}} = \mathbf{F}_{\mathrm{pl}}$. Substitution of (54) into (30) gives the following equation for the true DD tensor determined in relation to the GaAs reference structure,

$$\hat{\boldsymbol{\alpha}}_{\mathrm{GaAs}} = -(1+\hat{\boldsymbol{\beta}})^{-1}\overset{\mathrm{GaAs}}{\mathrm{Curl}}[(1+\hat{\boldsymbol{\beta}})], \tag{55}$$

where $\overset{\mathrm{GaAs}}{\mathrm{Curl}}$ denotes a pseudo-operator, cf. (15), concerning the local differentiation over a perfect lattice with the reference chemical composition. In terms of spatial gradients, cf. (15), this equation reads

$$\hat{\boldsymbol{\alpha}}_{\mathrm{GaAs}} = (1+\hat{\boldsymbol{\beta}})^{-1}\nabla(1+\hat{\boldsymbol{\beta}})^{\times}[(1+\hat{\boldsymbol{\beta}})^{-1}(1-\nabla\mathbf{u})]^{-\mathrm{T}}. \tag{56}$$

Substitution of $\mathbf{F}_{\mathrm{pl}'} = \mathbf{F}_{\mathrm{ch}}\mathbf{F}^{-1}_{\mathrm{o}}$ into (30) gives a DD tensor referred to the local relaxed lattice with the real chemical composition of sequential layers

$$\hat{\boldsymbol{\alpha}} = -\mathbf{F}_{\mathrm{ch}}(1+\widehat{\boldsymbol{\beta}})^{-1}\,\mathrm{Curl}[(1+\hat{\boldsymbol{\beta}})\mathbf{F}^{-1}_{\mathrm{ch}}]. \tag{57}$$

In terms of the gradients in the current configuration, this equation reads

$$\hat{\boldsymbol{\alpha}} = -\mathbf{F}_{\mathrm{ch}}(1+\widehat{\boldsymbol{\beta}})^{-1}\nabla[(1+\hat{\boldsymbol{\beta}})\mathbf{F}^{-1}_{\mathrm{ch}}] \overset{\times}{\cdot}[\mathbf{F}_{\mathrm{ch}}(1+\hat{\boldsymbol{\beta}})^{-1}(1-\nabla\mathbf{u})]^{-\mathrm{T}}. \tag{58}$$

FE algorithm proposed here is based on the integration of the equilibrium equation in the *current* configuration [30,31], i.e.

$$\mathrm{div}\,\boldsymbol{\sigma} = \mathbf{0}, \tag{59}$$

where the Cauchy stress tensor governed by the constitutive equation (47) is a nonlinear function of $\mathbf{u}$, $\nabla\mathbf{u}$, $\hat{\boldsymbol{\beta}}$ and $\nabla\hat{\boldsymbol{\beta}}$. Note that, according to (54) and (52) both total, lattice and plastic (rebuilding) deformation tensors, $\mathbf{F}$, $\mathbf{F}_{\mathrm{lt}}$ and $\mathbf{F}_{\mathrm{pl}}$ can be determined at any stage of the FE deformations. Using the virtual work principle the following nonlinear matrix equation is found

$$\mathbf{P}(\mathbf{a}) = \mathbf{f}, \tag{60}$$

where

$$\mathbf{P} = \begin{bmatrix} \int_v \nabla^{\mathrm{T}}\mathbf{W}\boldsymbol{\sigma}\,\mathrm{d}v \\ \mathbf{0} \end{bmatrix}, \quad \mathbf{a} = \begin{bmatrix} \mathbf{u} \\ \hat{\boldsymbol{\beta}} \end{bmatrix}, \quad \mathbf{f} = \begin{bmatrix} \int_{\partial v} \mathbf{W}\boldsymbol{\sigma}\,\mathrm{d}\mathbf{s} \\ \mathbf{0} \end{bmatrix}. \tag{61}$$

$\mathbf{W}$ denotes the weighting function determined in relation to the current (iterated) configuration. Fixing deformation freedom degrees corresponding to the lower row part of the matrix equation *its upper part was solved only*! Such a technique (with an undetermined lower equation for $\hat{\boldsymbol{\beta}}_i$) has been applied in order to obtain continuous, differentiable and mutually compatible fields $\mathbf{u}(\mathbf{x})$, $\mathbf{F}_{\mathrm{lt}}(\mathbf{x})$ and $\hat{\boldsymbol{\alpha}}(\mathbf{x})$. This is possible if the function $\mathbf{u}(\mathbf{x})$ is biquadratic, $\mathbf{F}(\mathbf{x})$, $\mathbf{F}_{\mathrm{lt}}(\mathbf{x})$, $\mathbf{F}_{\mathrm{pl}}(\mathbf{x})$ and $\hat{\boldsymbol{\beta}}(\mathbf{x})$ are bilinear, and $\mathbf{F}_{\mathrm{ch}}(\mathbf{x})$ is constant within elements. The spatial distribution of $\hat{\boldsymbol{\alpha}}(\mathbf{x})$ was shaped mainly by $\nabla N^{\beta}(\mathbf{x})$. For an arbitrarily chosen tensor field, say $\hat{\mathbf{t}}(\mathbf{x})$, the Curl pseudo-operator can be computed in the current configuration by using the global orthonormal coordinate set (laboratory system), i.e. $\mathrm{Curl}\,\hat{\mathbf{t}}_{\mathrm{ij}} = \hat{\mathbf{t}}_{\mathrm{ik,l}}F_{\mathrm{lt'lm}}e_{\mathrm{kmj}}$, see (15) and (37). In the computational process an orthonormal (laboratory) system was used, cf. mathematical forms of local and global shape gradient functions determined for the Gauss points in curvilinear finite elements, see [32].

Our FE algorithm is based upon the implicit method in which the differentiations are performed on the wanted configuration. The whole heterostructure has been divided into finite elements with a homogeneous chemical composition, see e.g. Fig. 9. In such a case, using the identity $\mathbf{F}^{-1}_{\mathrm{ch}} \times \mathbf{F}^{-\mathrm{T}}_{\mathrm{ch}} \det\mathbf{F}_{\mathrm{ch}} = \mathbf{F}_{\mathrm{ch}}\times$, Eq. (58) reduces to

$$\hat{\boldsymbol{\alpha}} = -\mathbf{F}_{\mathrm{ch}}(1+\hat{\boldsymbol{\beta}})^{-1}\nabla\hat{\boldsymbol{\beta}}^{\times}\left[(1+\hat{\boldsymbol{\beta}})^{-1}(1-\nabla\mathbf{u})\right]^{-\mathrm{T}} \mathbf{F}_{\mathrm{ch}}^{\mathrm{T}}\det\mathbf{F}_{\mathrm{ch}}^{-1}, \tag{62}$$

cf. the details of analogical transition (A.3) and (A.4) shown in Appendix A.

The upper part of the *nonsymmetric* equation set (60) was solved by using the Newton–Raphson method in which the tangent stiffness matrix takes form $\mathbf{K} = \frac{\partial \mathbf{P}}{\partial \mathbf{a}}$. In practice the following matrix was used

$$\mathbf{K}_{\mathrm{ij}} = \int_v \nabla N_i \frac{\partial(\boldsymbol{\sigma}\det\mathbf{F})}{\partial \mathbf{a}_{\mathrm{j}}}\det\mathbf{F}^{-1}\,\mathrm{d}v. \tag{63}$$

More details on the determination of the tangent matrix for nonlinear anisotropic elasticity elements are given in [30,31].

5.1. Interfacial stresses induced by elastic nonlinearity

According to the experimental data, the interfacial tension between thin layers takes often negative values from the domain −4 to 0 N/m [7]. On the other hand, according to classical thermodynamics, the surface energy and interfacial tension should be positive. The reason for negative surface tension lies in the elastic nonlinearity which make the compression region harder than extension. Therefore, the instantaneous stiffness of the extension and compression regions formed around an edge dislocation are mutually different. To balance the stresses, the extension region, as being more flexible, carries out most of the elastic incompatibility. Consequently, the overall lattice distortion around an edge dislocation is positive which manifests in the form of a positive volume expansion. In the first example a set of edge dislocations with mutually opposite Burgers vectors $\hat{\mathbf{b}} = \pm\frac{1}{2}[1\,\bar{1}\,0]$ in CdTe are assumed, see α_{xz} field Fig. 7. The assumed distance between dislocations was similar to that visible in Fig. 1. The dislocations were introduced into the FE mesh by the initial plastic deformation $\mathbf{F}_{\mathrm{pl_o}}(\mathbf{X}) = \mathbf{1} + \hat{\boldsymbol{\beta}}$. To avoid incompatibilities between the displacement and distortion fields within FEs the nine-node shape function $N_{\mathrm{i}}^{u}(\mathbf{x})$ for displacements and four-node (bilinear) shape function $N_{\mathrm{i}}^{\beta}(\mathbf{x})$ for lattice distortions were applied which gives

$$\mathbf{u}(\mathbf{x}) = \sum_{\mathrm{i}=1,9} N_{\mathrm{i}}^{u}(\mathbf{x})\mathbf{u}_{\mathrm{i}}, \tag{64}$$

$$\hat{\boldsymbol{\beta}}(\mathbf{x}) = \sum_{\mathrm{i}=1,4} N_{\mathrm{i}}^{\beta}(\mathbf{x})\hat{\boldsymbol{\beta}}_{\mathrm{i}}, \tag{65}$$

where $\mathbf{u}_{\mathrm{i}}$, and $\hat{\boldsymbol{\beta}}_{\mathrm{i}}$ are nodal variables. This implies that the source distortions were input only to four corner nodes while the displacements were wanted for all nine nodes. In the 2D boundary-value problem, the lattice disordered regions were recognized by using the following formula $\hat{\alpha} = \sqrt{\hat{\alpha}_{xz}^2 + \hat{\alpha}_{yz}^2}$, see (47). The dislocation core parameter assumed here was $r = 20$. Solving the boundary-value problem the equilibrium configurations of mesh were determined for several values of the strain parameter m for $\widehat{\mathbf{C}} = 0$. This parameter is responsible for the asymmetry in elastic hardening between the extension and compression behaviour and takes a similar role as the third-order elastic constants, see transformation rule for the third-

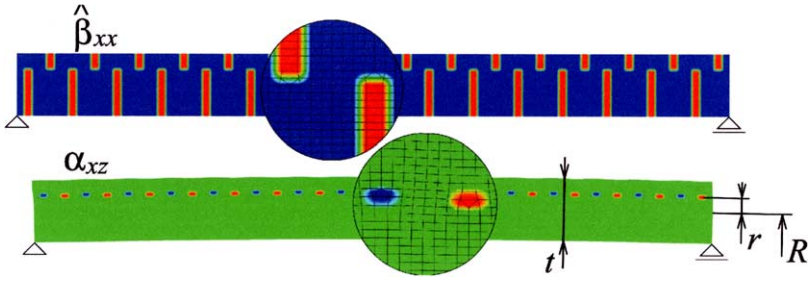

Fig. 7. Boundary-value problem for dislocation zone in CdTe: contour maps of $\hat{\beta}_{xx}$ and α_{xz} shown in the initial and stress-equilibrium configurations, respectively.

order elastic constants (39), (46) and Table 1. Therefore, the resulting curvature of the FE mesh depended on the assumed value of m, see Fig. 7. To express this curvature in terms of interfacial stress resolved in the dislocation zone the analogical formula as that applied by experimenters is used to measure interfacial tension, i.e. $f \approx \frac{Eh^3}{6(1-\nu)tR}$, where E, ν are elastic constants, R, t and h determine the geometry of the FE mesh. Such determined dependency f versus m is shown in Fig. 8. To be in agreement with the experimental data reported by Spaepen the strain parameter to be assumed must be in the domain -2 to -4, see Fig. 8. But in the real interfacial regions, the total number of dislocations can significantly overcome the number of geometrically necessary dislocations. Therefore, the significantly smaller elastic asymmetry may induce the curvature observed experimentally. Comparing the curvature obtained in this example with the experimentally determined third-order elastic constants, cf. Table 1, it is expected that the strain parameter should be chosen rather from the domain $-1 < m < 0$.

5.2. 2D stress problem for misfit dislocations

In this example the lattice distortion field $\hat{\boldsymbol{\beta}}(\mathbf{x}^{\mathrm{HRTEM}})$ extracted from the HRTEM image (see Figs. 1 and 3) was used as the input data to the FE analysis. The image was recorded in the form of a 1024×1024 bitmap, see Figs. 1 and 3. After rejecting a boundary zone, the central region of the image was taken as input data to FE analysis, 964 px$\times$964 px. The whole region was divided into 10 000 nine-node square elements, see Fig. 9. The source distortions were applied only in the corner nodes, cf. (65). The nodal values $\hat{\beta}_{\mathrm{i}}$ were determined by averaging the distortions $\boldsymbol{\beta}^{\mathrm{HRTEM}}$ over all pixels situated near a given node, and then transforming $\beta_{\mathrm{i}}^{\mathrm{HRTEM}}$ into $\hat{\beta}_{\mathrm{i}}$, see (53). In the initial configuration, each of FEs occupied a square region 9 px$\times$9 px, i.e. $\frac{3}{8}\hat{a}_{\mathrm{GaAs}} \times \frac{3}{8}\hat{a}_{\mathrm{GaAs}}$. The assumed mesh is shown in Fig. 9. A free boundary condition was assumed. The left-lower corner of the mesh was fixed and the right-lower corner was constrained in the y-direction. This implies that the solution obtained relates to the residual stresses stored in the interior of the considered region. This FE analysis corresponds to the cutting of the examined crystal region out from a larger sample and relaxing it according to the assumed free boundary condition. The following material constants were assumed: $\hat{a}_{\mathrm{CdTe}} = 6.48$ Å, $\hat{a}_{\mathrm{ZnTe}} = 6.1034$ Å, $\hat{a}_{\mathrm{GaAs}} = 5.6530$ Å, $r = 20$, the second and third-order elastic constants for logarithmic strain are given in Table 1. The solution process was not as stable as that for the regular distortion field considered in Example 1. Taking only the traditional elastic constants into account a good convergence (10^{-10}) was obtained in the domain $-4 < m < +1.5$. This means that for outside values (including Green strain) the possible stress-equilibrium configuration was too far from the initial (HRTEM) configuration and it was not reachable by using the modified Newton–Raphson method. For this reason the final calculations were carried out by using the logarithmic strain. The resulting residual stresses are shown in Fig. 9.

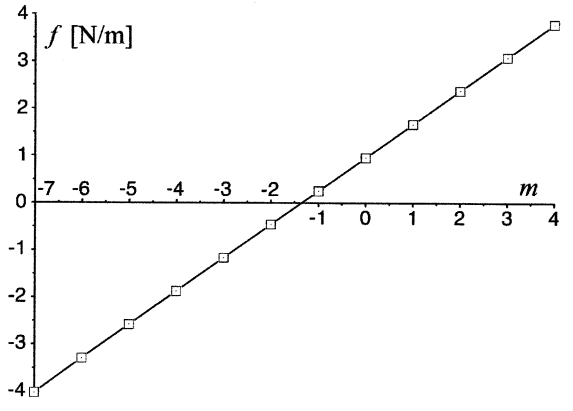

Fig. 8. Surface tension obtained by solving a FE problem, Fig. 7, in which the elastic hardenning was controlled only by the strain parameter m, cf. (47) and (39).

5.3. 3D problem for 60° dislocations

The computational technique proposed here gives some possibilities to solve a 3D boundary-value problem with screw components. 3D FE problems are considerably more memory intensive than 2D. With respect to the limited computer capabilities and to maintain a good resolution of stress and displacement, maps only a fragment of

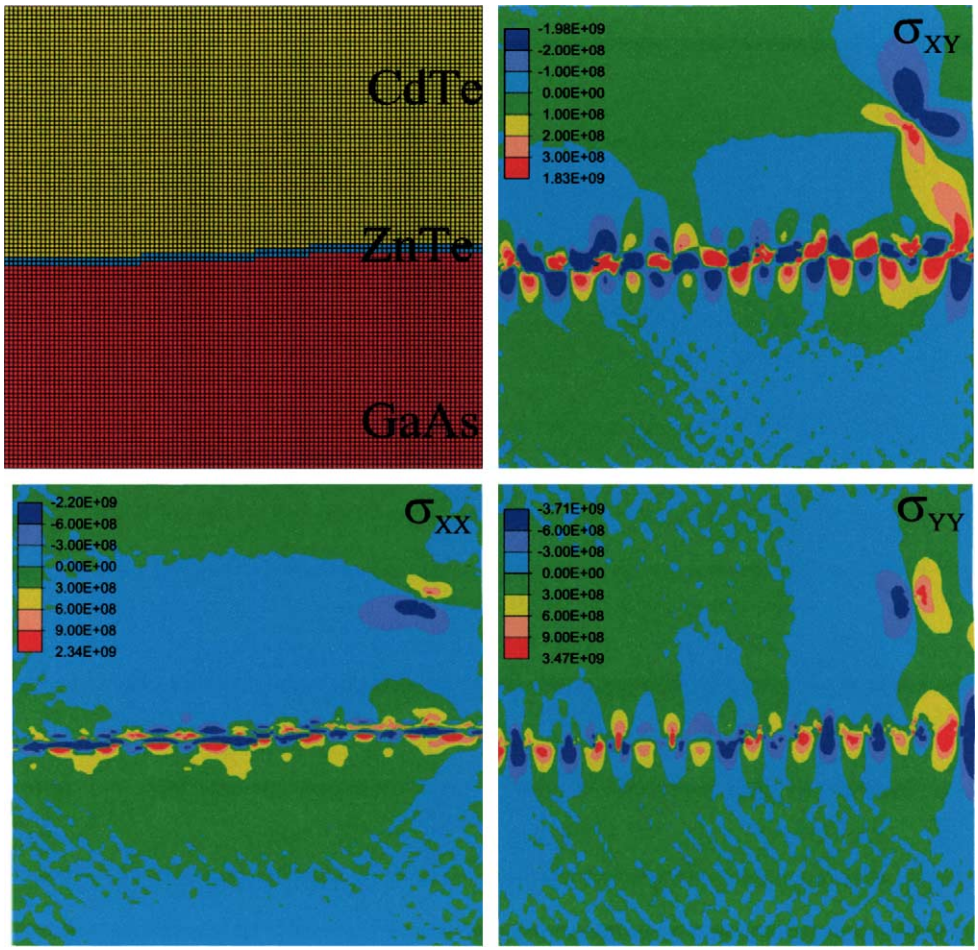

Fig. 9. Assumed mesh and residual stresses obtained by solving nonlinear 2D FE problem.

the HRTEM image was taken into a 3D analysis. A new region of the HRTEM image chosen for the 3D calculation was located outside the image shown in Fig. 1. It contained a single 60° misfit dislocation and a single edge dislocation $\frac{1}{2}[1\,\bar{1}\,0]$ which had parted into two elemental 60° dislocations, see the DD tensor field in Fig. 10. Their Burgers vectors were $\frac{1}{2}[1\,0\,\bar{1}]$ and $\frac{1}{2}[0\,\bar{1}\,1]$, or $\frac{1}{2}[1\,0\,1]$ and $\frac{1}{2}[0\,\bar{1}\,\bar{1}]$, respectively. In this example the first case was considered. The assumed Burgers vectors decompose into the following x, y, z-components

$$\begin{aligned}\tfrac{1}{2}[1\,0\,\bar{1}] &= \tfrac{1}{4}[1\,\bar{1}\,0] + \tfrac{1}{2}[0\,0\,\bar{1}] + \tfrac{1}{4}[1\,1\,0],\\ \tfrac{1}{2}[0\,\bar{1}\,1] &= \tfrac{1}{4}[1\,\bar{1}\,0] - \tfrac{1}{2}[0\,0\,\bar{1}] - \tfrac{1}{4}[1\,1\,0].\end{aligned} \tag{66}$$

Note, that z- and y-components satisfy a linear dependence $\hat{b}_3 = \frac{\sqrt{2}}{2}\hat{b}_2$. Therefore, in this example the source distortions have been assumed to be

$$[\hat{\boldsymbol{\beta}}] = \begin{bmatrix} \hat{\beta}_{11} & \hat{\beta}_{12} & 0 \\ \hat{\beta}_{21} & \hat{\beta}_{22} & 0 \\ \frac{\sqrt{2}}{2}\hat{\beta}_{21} & \frac{\sqrt{2}}{2}\hat{\beta}_{22} & 0 \end{bmatrix}, \tag{67}$$

where

$$\begin{bmatrix} \hat{\beta}_{11} & \hat{\beta}_{12} \\ \hat{\beta}_{21} & \hat{\beta}_{22} \end{bmatrix} = \begin{bmatrix} 1-\beta_{11}^{\mathrm{HRTEM}} & -\beta_{12}^{\mathrm{HRTEM}} \\ -\beta_{21}^{\mathrm{HRTEM}} & 1-\beta_{22}^{\mathrm{HRTEM}} \end{bmatrix}^{-1} - [\mathbf{1}], \tag{68}$$

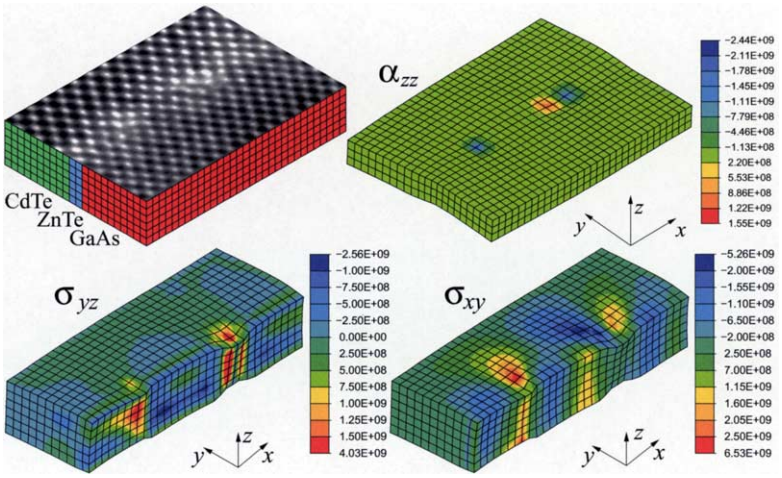

Fig. 10. 3D FE problem for 60° dislocations extracted from HRTEM image: assumed mesh, screw DD component α_{zz} and residual stresses, σ_{yz} and σ_{yz}, shown in cross-sections.

cf. (53). It is easy to note that such chosen distortions lead to the following nonvanishing components of the DD tensor: $\hat{\alpha}_{13}, \hat{\alpha}_{23}$ and $\hat{\alpha}_{33}$, where $\hat{\alpha}_{33} = \frac{\sqrt{2}}{2}\hat{\alpha}_{23}$, cf. (30). In this example, the tensor invariant $\hat{\alpha}$ used in the constitutive equation (47) was determined as $\hat{\alpha} = \sqrt{\hat{\alpha}_{xz}^2 + \hat{\alpha}_{yz}^2 + \hat{\alpha}_{zz}^2}$. Solving the FE problem for free boundary conditions, the residual stresses shown in Fig. 10 were obtained. The field σ_{yz} is induced mainly by the screw components of the dislocations. Nevertheless some additional shear effects appeared in the boundary zone. They resulted from the width changes because in the transit region between the GaAs and CdTe layers the free surfaces of the sample were not exactly perpendicular to the z-axis which means that the shear stress σ_{yz} had not to vanish at the slant surfaces.

6. Summary

The aim of this paper was to show the theoretical and numerical foundations of a new method for computer analysis of residual stresses in nanostructures examined under microscope. From the theoretical point of view, the computational method proposed can be used on-line during HRTEM examination. Using the tensor field extracted directly from the experimental image many questions arise, e.g. concerning the reality of experimental results, assumed nonlinearity of the constitutive model, boundary conditions, etc. The problem of nonlinearity can be divided into two subproblems: (a) the geometric nonlinearity relating to the unique description of sequential configurations in space and (b) to the constitutive nonlinearity. In our case, both subproblems were taken into account in a fully nonlinear FE code.

The surface tension was considered in terms of a 3D stress equilibrium of a misfit dislocation zone. As was shown, due to asymmetry in the stress–strain response of compression and extension regions, the volume expansion and interfacial tension depended strongly on the elastic nonlinearity.

The computer method applied here can be used not only to HRTEM but also to any other experimental method allowing the extraction of nano/pico-continuous distortion maps from examined atomic structures. The important advantage of the nonlinear description is the possibility of recovering a deformed atomic structure from distortion maps. Contrary to the linear theory, it is possible to reconstruct the lattice by departing from any atomic position and integrating the 3D distortion field step-by-step according to the state-of-the-art of nonlinear theory of crystal deformations, cf. (16) and (34).

Acknowledgements

This research was supported by the State Committee for Scientific Research (KBN) in Poland under grant no. 4 T11F 008 25. The sample for HRTEM investigations has been made in GGPLDSC IP-PAS in Warszawa, while the investigations have been carried out in collaboration with LPS-ESPCI in Paris.

Appendix A

A.1. Discussion of (3)

Let us consider the proof of (3) in terms of curvilinear coordinate sets.

$$\begin{aligned}\mathbf{F}_{,L} &= \frac{\partial}{\partial X^L}\left(\frac{\partial x^k}{\partial X^K}\mathbf{e}_k \otimes \mathbf{E}^K\right)\\ &= \frac{\partial^2 x^k}{\partial X^K \partial X^L}\mathbf{e}_k \otimes \mathbf{E}^K + \frac{\partial x^k}{\partial X^K}\frac{\partial \mathbf{e}_k}{\partial X^L}\otimes \mathbf{E}^K\\ &\quad + \frac{\partial x^k}{\partial X^K}\mathbf{e}_k \otimes \frac{\partial \mathbf{E}^K}{\partial X^L}\\ &= \frac{\partial^2 x^k}{\partial X^K \partial X^L}\mathbf{e}_k \otimes \mathbf{E}^K + \frac{\partial x^k}{\partial X^K}\frac{\partial x^l}{\partial X^L}\frac{\partial \mathbf{e}_k}{\partial x^l}\otimes \mathbf{E}^K\\ &\quad + \frac{\partial x^k}{\partial X^K}\mathbf{e}_k \otimes \frac{\partial \mathbf{E}^K}{\partial X^L}\\ &= \left(\frac{\partial^2 x^k}{\partial X^K \partial X^L} + \frac{\partial x^m}{\partial X^K}\frac{\partial x^l}{\partial X^L}\Gamma^k_{ml}\right.\\ &\quad \left. + \frac{\partial x^k}{\partial X^M}(-\Gamma^K_{ML})\right)\mathbf{e}_k \otimes \mathbf{E}^K, \end{aligned} \tag{A.1}$$

where $\Gamma^k_{ml} \overset{\mathrm{d}f}{=} \frac{\partial \mathbf{e}_m}{\partial x^l}\cdot \mathbf{e}^k = -\mathbf{e}_m \cdot \frac{\partial \mathbf{e}^k}{\partial x^l}$ and $\Gamma^K_{ML} \overset{\mathrm{d}f}{=} \frac{\partial \mathbf{E}_M}{\partial X^L}\cdot \mathbf{E}^K = -\mathbf{E}_K \cdot \frac{\partial \mathbf{E}^M}{\partial X^L}$. The connection coefficients satisfy the well-known conditions $\Gamma^k_{ml}\mathbf{e}_k = \frac{\partial \mathbf{e}_m}{\partial x^l}$, $\Gamma^k_{ml}\mathbf{e}^m = -\frac{\partial \mathbf{e}^k}{\partial x^l}$, $\Gamma^K_{ML}\mathbf{E}_K = \frac{\partial \mathbf{E}_M}{\partial X^L}$ and $\Gamma^K_{ML}\mathbf{E}^M = -\frac{\partial \mathbf{E}^K}{\partial X^L}$. This means that

$$\begin{aligned}\mathbf{F}_{,L}\times \mathbf{E}^L &= \left(\frac{\partial^2 x^k}{\partial X^K \partial X^L} + \frac{\partial x^m}{\partial X^K}\frac{\partial x^l}{\partial X^L}\Gamma^k_{ml}\right.\\ &\quad \left. - \frac{\partial x^k}{\partial X^M}\Gamma^K_{ML}\right)\mathbf{e}_k \otimes \mathbf{E}^K \times \mathbf{E}^L\\ &= \left(\frac{\partial^2 x^k}{\partial X^K \partial X^L} + \frac{\partial x^m}{\partial X^K}\frac{\partial x^l}{\partial X^L}\Gamma^k_{ml}\right.\\ &\quad \left. - \frac{\partial x^k}{\partial X^M}\Gamma^K_{ML}\right)e^{KL}_M \mathbf{e}_k \otimes \mathbf{E}^M, \end{aligned} \tag{A.2}$$

where e^{KL}_M denotes the respective representation of the alternating tensor of E^3 [20,33]. Contrary to non-Riemannian spaces, in E^3 the vector basis tangent to $\{x^k\}$ is holonomic, i.e. there exist a position vector, say $\mathbf{r}$, such that each element of a vector basis has to satisfy the condition $\mathbf{e}_k = \frac{\partial \mathbf{r}}{\partial x^k}$. In view of the definition of Γ^K_{ML} following (A.1), the holonomy implies the symmetry of connection coefficients. Thus, because of $\frac{\partial^2 x^k}{\partial X^K \partial X^L} = \frac{\partial^2 x^k}{\partial X^L \partial X^K}$, $\Gamma^k_{ml} = \Gamma^k_{lm}$ and $\Gamma^K_{ML} = \Gamma^K_{LM}$, (3b) is obtained.

A.2. Comments to (23), (30) and (32)

Substitution of (8) into (23) gives

$$\begin{aligned}\hat{\alpha}^{KN} &= \overset{-1}{F}{}_{\mathrm{lt}}{}^K{}_{k,m} e^{kmn} \overset{-1}{F}{}_{\mathrm{lt}}{}^N{}_n \det \mathbf{F}_{\mathrm{lt}}\\ &= -F_{\mathrm{pl}}{}^K{}_A \overset{-1}{F}{}_{\mathrm{pl}}{}^A{}_{B,m} \overset{-1}{F}{}_{\mathrm{lt}}{}^B{}_k e^{mkn} \overset{-1}{F}{}_{\mathrm{lt}}{}^N{}_n \det \mathbf{F}_{\mathrm{lt}}. \end{aligned} \tag{A.3}$$

Note, that $\overset{-1}{F}{}_{\mathrm{lt}}{}^B{}_k \overset{-1}{F}{}_{\mathrm{lt}}{}^N{}_n e^{mkn} e_{BNM}$ is the adjoint of $\mathbf{F}^{-1}_{\mathrm{lt}}$. Since the inverse of a given second-order tensor is determined as $\mathbf{t}^{-1} = \frac{\mathrm{adj}\mathbf{t}}{\det \mathbf{t}}$, thus $\overset{-1}{F}{}_{\mathrm{lt}}{}^B{}_k e^{mkn} \overset{-1}{F}{}_{\mathrm{lt}}{}^N{}_n \det \mathbf{F}_{\mathrm{lt}} = F_{\mathrm{lt}}{}^m{}_K e^{KBN}$. Substituting this relation into (A.3) we find

$$\begin{aligned}&-F_{\mathrm{pl}}{}^K{}_A \overset{-1}{F}{}_{\mathrm{pl}}{}^A{}_{B,m} \overset{-1}{F}{}_{\mathrm{lt}}{}^B{}_k e^{mkn} \overset{-1}{F}{}_{\mathrm{lt}}{}^N{}_n \det \mathbf{F}_{\mathrm{lt}}\\ &\quad = -F_{\mathrm{pl}}{}^K{}_A \overset{-1}{F}{}_{\mathrm{pl}}{}^A{}_{B,m} F^m{}_C \overset{-1}{F}{}_{\mathrm{pl}}{}^C{}_D e^{DBN}\\ &\quad = F_{\mathrm{pl}}{}^K{}_{A,m} \overset{-1}{F}{}_{\mathrm{pl}}{}^A{}_B F^m{}_C \overset{-1}{F}{}_{\mathrm{pl}}{}^C{}_D e^{DBN}\\ &\quad = F_{\mathrm{pl}}{}^K{}_{A,m} F^m{}_C \overset{-1}{F}{}_{\mathrm{pl}}{}^A{}_B \overset{-1}{F}{}_{\mathrm{pl}}{}^C{}_D e^{DBN}\\ &\quad = F_{\mathrm{pl}}{}^K{}_{A,m} F^m{}_L F_{\mathrm{pl}}{}^N{}_E e^{EAL} \det \mathbf{F}^{-1}_{\mathrm{pl}}\\ &\quad = F_{\mathrm{pl}}{}^K{}_{A,L} e^{ALE} F_{\mathrm{pl}}{}^N{}_E \det \mathbf{F}^{-1}_{\mathrm{pl}}. \end{aligned} \tag{A.4}$$

The two last terms are just the index representations of (30) and (32), respectively.

References

[1] M.J. Hÿtch, J.-L. Putaux, J.-M. Pénisson, Measurement of the displacement field of dislocations to 0.03 Å by electron microscopy, Nature 423 (15) (2003) 270–273.
[2] M.J. Horodon, B.L. Averbach, Acta Metall. 9 (1961) 247.
[3] P. Dłużewski, Anisotropic hyperelasticity based upon general strain measures, J. Elasticity 60 (2) (2000) 119–129.
[4] S.N. Vaidya, G.C. Kennedy, Compressibility of 18 metals to 45 kb, J. Phys. Chem. Solids 31 (1970) 2329–2345.

[5] S.N. Vaidya, G.C. Kennedy, Compressibility of 22 elemental solids to 45 kb, J. Phys. Chem. Solids 33 (1972) 1377–1389.
[6] M.W. Guinan, D.J. Steinberg, Pressure and temperature derivatives of the isotropic polycrystalline shear modulus for 65 elements, J. Phys. Chem. Solids 35 (1974) 1501–1512.
[7] F. Spaepen, Interfaces and stresses in thin films, Acta Mater. 48 (2000) 31–42.
[8] G.R. Canova, Y. Brechet, L.D. Kubin, B. Devincre, V. Pontikis, 3D simulation of dislocation motion on a lattice: application to the yield surface of single crystals, Solid State Phenom. 35–36 (1994) 101–106.
[9] C. Lemarchand, B. Devincre, L.P. Kubin, Homogenization method for a discrete-continuum simulation of dislocation dynamics, J. Mech. Phys. Solids 49 (9) (2001) 1969–1982.
[10] H.M. Zbib, M. Rhee, J.P. Hirth, On plastic deformation and the dynamics of 3D dislocations, Int. J. Eng. Sci. 2–3 (1998) 113–127.
[11] K.W. Schwarz, D. Chidambarrao, Dislocation dynamics near film and corners in silicon, J. Appl. Phys. 85 (10) (1999) 7198–7208.
[12] S. Kolling, R. Mueller, D. Gross, A computational concept of the kinetics of defects in anisotropic materials, Comput. Mater. Sci. 26 (2003) 87–94.
[13] T.T. Cheng, M. Aindow, I.P. Jones, J.E. Hails, D.J. Williams, The role of the initial nucleation stage in microstructural development for CdTe grown on heat-cleaned 2 degrees-off (0 0 1)GaAs by metalorganic chemical vapour deposition, J. Cryst. Growth 154 (3–4) (1995) 251–261.
[14] M.J. Hÿtch, E. Snoeck, R. Kilaas, Quantitative measurement of displacement and strain fields from HTEM micrographs, Ultramicroscopy 74 (1998) 131–146.
[15] S. Kret, P. Dłużewski, P. Dłużewski, J.-Y. Laval, On the measurement of dislocation cores distribution in GaAs/ZnTe/CdTe heterostructure by transmission electron microscopy, Philos. Mag. A 83 (2003) 231.
[16] K. Kondo, On geometrical and physical foundations of the theory of yielding, in: Proc. 2nd Japan Nat. Congr. Appl. Mech, vol. 2, 1952, pp. 41–47.
[17] B.A. Bilby, Continuous distribution of dislocations, in: I.N. Sneddon, R. Hill (Eds.), Progress in Solid Mechanics, vol. 1, North-Holland, Amsterdam, 1960, pp. 331–398.
[18] K. Kondo, Non-Riemannian and Finslerian approaches to the theory of yielding, Int. J. Eng. Sci. 1 (1963) 71–88.
[19] J.P. Hirth, J. Lothe, Theory of Dislocations, Wiley, New York, 1982.
[20] P. Dłużewski, Continuum theory of dislocations as a theory of constitutive modelling of finite elastic–plastic deformations, Habilitation Thesis, IFTR Reports 13/1996, Warsaw, 1996.
[21] P. Dłużewski, On geometry and continuum thermodynamics of movement of structural defects, Mech. Mater. 22 (1) (1996) 23–41.
[22] Y. Hiki, A.V. Granato, Anharmonicity in noble metals; higher order elastic constants, Phys. Rev. 144 (2) (1966) 411–419.
[23] J.R. Drabble, A.J. Brammer, Third-order elastic constants of gallium arsenide, Solid State Commun. 4 (9) (1966) 467–469.
[24] C. Teodosiu, Elastic Models of Crystal Defects, Springer-Verlag and Editura Academiei, Berlin and Bucureşti, 1982.
[25] B.R. Seth, Generalized strain measure with applications to physical problems, in: M. Reiner, D. Abir (Eds.), Second-Order Effects in Elasticity, Plasticity and Fluid Dynamics, Pergamon Press, Oxford, 1964, Proc. Int. Sympos., Haifa, April 23–27, 1962.
[26] R. Hill, Constitutive inequalities for isotropic solids under finite strain, Proc. R. Soc. London A 314 (1970) 457–472.
[27] K. Brugger, Thermodynamic definition of higher order elastic coefficients, Phys. Rev. 133 (6A) (1964) 1611–1612.
[28] R.N. Thurston, K. Brugger, Third-order elastic constants and the velocity of small amplitude elastic waves in homogeneously stressed media, Phys. Rev. 133 (6A) (1964) 1604–1610.
[29] N.J. Walker, G.A. Saunders, J.E. Hawkey, Soft TA models and anharmonicity in cadmium telluride, Phys. Rev. B 52 (5) (1985) 1005–1018.
[30] P. Dłużewski, P. Rodzik, Elastic eigenstates in finite element modelling of large hyper-elastic deformations, Comput. Methods Appl. Mech. Eng. 160 (3–4) (1998) 325–335.
[31] P. Dłużewski, G. Jurczak, H. Antúnez, Logarithmic measure of strains in finite element modelling of anisotropic deformations of elastic solids, Comput. Assisted Mech. Eng. Sci. 10 (2003).
[32] O.C. Zienkiewicz, R.J. Taylor, in: The Finite Element Method, fourth ed., vol. 1, McGraw-Hill, London, 1989.
[33] C. Eringen (Ed.), Continuum Physics, vol. II, Academic Press, 1975.
[34] R.K. Singh, S. Singh, Study of elastic properties and their pressure dependence of zincblende structure semiconductors, Phys. Stat. Sol. (b) 140 (1987) 407–412.